Journal of Molecular Catalysis A: Chemical 326 (2010) 1–7

Contents lists available at ScienceDirect

Journal of Molecular Catalysis A: Chemical

journal homepage: www.elsevier.com/locate/molcata

Editor choice paper

A visible light active photocatalyst: Nano-composite with Fe-doped anatase TiO_2 nanoparticles coupling with TiO_2(B) nanobelts

Lifeng Cui, Feng Huang, Mutong Niu, Lingwei Zeng, Ju Xu, Yuansheng Wang*

State Key Laboratory of Structural Chemistry, Fujian Institute of Research on the Structure of Matter, Chinese Academy of Sciences, Graduate University of Chinese Academy of Sciences, Fuzhou, Fujian 350002, China

ARTICLE INFO

Article history:
Received 2 February 2010
Received in revised form 16 April 2010
Accepted 22 April 2010
Available online 20 May 2010

Keywords:
Anatase TiO_2
Fe doping
TiO_2(B)
Nano-composite
Photocatalysis

ABSTRACT

The nano-composite photocatalyst with Fe-doped anatase TiO_2 nanoparticles (5–10 nm in size) coupling with TiO_2(B) – an uncommon synthetical polymorph of titanium oxide with monoclinic structure – nanobelts (30–100 nm in width, 10–30 nm in thickness, and several micrometers in length) was fabricated via a two-step procedure: hydrothermal synthesis of the TiO_2(B) nanobelts followed by co-deposition of the Fe-doped anatase TiO_2 nanoparticles on the nanobelts. The microstructure and photocatalysis of the samples were systematically studied by TEM, HRTEM, EDS, XRD, UV–vis and BET techniques. The purpose of the coupling of different TiO_2 polymorphs is to accelerate the separation of photogenerated charges and improve the photon quantum efficiency. The Fe doping endows the TiO_2 based nano-composite with visible light photocatalytic activity. An efficient photodegradation of the methyl orange aqueous solution was achieved under visible light ($\lambda > 420$ nm) irradiation, revealing the potential applicability of such nano-composite in some industrial fields, such as air and water purifications.

1. Introduction

TiO_2 has been considered as an excellent photocatalyst in degrading a large variety of environmental contaminants, such as organic materials, bacteria, and viruses, for its nontoxicity, cheapness, and chemical stability [1–7]. However, it is unavoidable to face two issues for its practical applications, one is to improve the low photon quantum efficiency of TiO_2 that arises from the fast recombination of photogenerated carriers; and the other is to further extend its photoresponse into visible light regions. Previous studies indicated that coupling of different crystalline TiO_2 phases (anatase, rutile, brookite, TiO_2(B), and so on) can improve the charge separation of the photogenerated carriers, resulting in the enhancement of the photocatalytic activity [8–13]. For example, Degussa P25, the most commonly used photocatalyst in commerce, is a mixture of anatase and rutile which exhibits much higher photocatalytic activity than the pure anatase or rutile photocatalyst [14–16]. Zhang and coworkers synthesized a kind of mixed-phase TiO_2 nanocrystals with tunable brookite-to-rutile ratio, and found that the maximum activity was about six times of that of Degussa P25 for the degradation of Rhodamine B in an aqueous solution [17]. Zhu et al. reported a photocatalyst mixed with TiO_2(B) and anatase phases, and demonstrated the charge transfer at the interfaces under the UV light irradiation [11]. As we know, anatase TiO_2 is a wide bandgap semiconductor with bandgap energy of 3.2 eV, capable of utilizing only the UV light. The bandgap energy modification of TiO_2 through the transition metal doping is a feasible way to realize its optical characteristic modulation. The Fe-doped TiO_2 nanoparticles have been widely reported to have visible light photocatalytic activity due to the introducing of impurity levels into the TiO_2 bandgap [18].

TiO_2 crystallizes in three natural crystalline polymorphs: anatase ($I4_1/amd$), rutile ($P4_2/mnm$) and brookite ($Pbca$), and five synthetical polymorphs: TiO_2(B) ($C2/m$), TiO_2-R ($Pbnm$), TiO_2-H ($I4/m$), TiO_2-II ($Pbcn$) and TiO_2-III ($P2_1/c$) [19,20]. For the two most common polymorphs, anatase generally shows better performances than its rutile counterpart in photocatalytic applications [3]. The others are relatively less studied, mainly owing to the difficulties in preparation. As a very uncommon crystalline phase, monoclinic TiO_2(B), with a shear derivative of the ReO_3 type structure, is an n-type semiconductor possessing some unique electrochemical and catalytic properties compared to the other TiO_2 polymorphs [21–23]. Recently, Lee and coworkers studied the photocatalytic activity of TiO_2(B), and found that it was similar to that of Degussa P25 because of the negatively charged titania blocks that enhance the adsorption affinity toward organic compounds [24].

In this paper, we report a nano-composite with Fe-doped anatase TiO_2 nanoparticles (denoted as Fe–TiO_2 NPs) coupling with TiO_2(B) nanobelts (denoted as TiO_2 NBs) which exhibits excellent visible light photocatalytic activity.

* Corresponding author. Tel.: +86 591 83705402, fax: +86 591 83705402.
E-mail address: yswang@fjirsm.ac.cn (Y. Wang).

1381-1169/$ – see front matter © 2010 Elsevier B.V. All rights reserved.
doi:10.1016/j.molcata.2010.04.013

2. Experimental

2.1. Synthesis of nano-composite

All the chemicals used were purchased from Sinopharm Chemical Reagent Co. Ltd., China. The nano-composite was prepared by a two-step procedure. Firstly, the TiO_2 NBs with rough porous structure on the surface to provide more reactive sites were synthesized hydrothermally in a concentrated alkali solution. The doping of Fe in TiO_2 NPs and the coupling between TiO_2 NPs and TiO_2 NBs were proceeded synchronously by a co-deposition reaction of titanium sulfate and iron nitrate in the hot acidic aqueous solution at the presence of TiO_2 NBs as the precursor, followed by a calcining treatment.

The preparation of TiO_2 NBs followed a modified route reported by Kasuga et al. [25]. In a typical experiment, 1.0 g amorphous TiO_2 ≥99%) white powders were placed into a Teflon-lined autoclave of 50 mL capacity. Then, the autoclave was filled with 40 mL NaOH (≥96%) (10 M) aqueous solution, sealed into a stainless steel tank and maintained at 180 °C for 36 h without shaking or stirring during the heating. After the autoclave was naturally cooled to room temperature, the obtained sample was sequentially washed by dilute HCl aqueous solution, distilled deionized water and absolute ethanol for several times. After drying at 80 °C for 6 h followed by calcining at 500 °C for 5 h, the final soft fibrous powders with white color were obtained.

For the fabrication of Fe–TiO_2 NPs/TiO_2 NBs nano-composite, 0.2 g TiO_2 NBs and 0.056 g sodium dodecyl sulfate (≥96%), an organic ligand acting as the stabilizing agent, were firstly put into a 50 mL beaker containing 6 mL H_2O, and the pH of the solution was modulated to 2.0–3.0 by sulfuric acid (95–98%) to slow down the co-precipitation rate of titanium(IV)-oxide-hydroxide and iron(III) hydroxide. Then, 10 mL aqueous solution containing certain amounts of titanium(IV) sulfate (≥96%) and iron(III) nitrate nonahydrate (≥98.5%) were added into the above beaker in drops under stirring at the temperature of 100 °C. After reaction, the composite product was filtrated, washed with deionized water and dried at 120 °C for 2 h, and finally calcined at 500 °C for another 5 h. The heat treatments were carried out in a muffle type furnace (200 mm × 120 mm × 80 mm in dimension) in still air, and the heating rate was set to 10 °C/min. To simplify the denotation of the composites with different compositions, the as-prepared powders are named as *x*Fe–*y*TiO_2 NPs/TiO_2 NBs, where *x* is the nominal atomic ratio of Fe to Ti in Fe–TiO_2 NPs, and *y* the mass percentage of TiO_2 NPs in the TiO_2 NPs/TiO_2 NBs composite.

2.2. Characterization of nano-composite

The crystalline phases of the synthesized samples were determined by powder X-ray diffraction (XRD) on a Rigaku D/MAX2500 diffractometer with copper *K*α (λ = 0.154 nm) radiation. The morphology, microstructure and composition were investigated by transmission electron microscopy (TEM, JEM-2010) equipped with energy dispersive X-ray spectroscopy (EDS). The UV–vis diffuse reflectance spectra were detected by a spectrometer (Lambda 900). The surface area measurements were carried out on a Surface Area and Porosity Analyzer (ASAP2020C+M), using the Brunauer–Emmett–Teller (BET) technique. Desorption isotherms were measured to determine the pore size distribution and the pore diameter using the Barret–Joyner–Halender (BJH) method.

2.3. Photocatalytic measurements

To characterize the photocatalytic activity of the nano-composite under visible light irradiation, measurements on photodegradation of methyl orange (MO) in the model waste water were carried out at room temperature. For each experiment, 100 mg nano-composite was put in a beaker containing 50 mL 10^{-5} M MO water solution. A 500 W tungsten iodide lamp with a cut-off filter to remove the radiation below 420 nm was used as the visible light source. The solution was magnetically stirred for 3 h in dark to establish an adsorption/desorption equilibrium of MO on the surfaces of the catalyst, then the light was turned on to initiate the photocatalytic reaction. After irradiation for 5 h, the suspension was extracted and centrifuged at the rate of 6000 rpm for 5 min to remove the catalyst. The concentrations of MO before and after photocatalytic degradation were calibrated by the intensity of its characteristic absorption peak located at 496 nm measured with a UV–vis spectrometer (Lambda 35).

3. Results and discussion

3.1. Microstructure of nano-composite

XRD pattern of the TiO_2 NBs exhibits an uncommon monoclinic crystalline structure (JCPDS 46-1237), as shown in Fig. 1a; while in that of the 0.015Fe–50%TiO_2 NPs/TiO_2 NBs composite presented in Fig. 1a, besides the original peaks from TiO_2(B), there are some other peaks ascribing to the anatase TiO_2 (JCPDS 73-1764). Noticeably, no any other Fe-contained crystalline phase is detected.

TEM and high-resolution TEM (HRTEM) images in Fig. 2 show the morphology and microstructure of the TiO_2 NBs. Fig. 2a exhibits the well-dispersed TiO_2 NBs with 30–100 nm in width and several micrometers in length. Their thicknesses were measured to be in the range of 10–30 nm by TEM tilting observations. The magnified TEM micrograph taken from a TiO_2 NB, as shown in Fig. 2b, reveals the porous feature with pore size ranging from several to dozens nanometers on the surface of the nanobelt. The HRTEM image taken from the marked region in Fig. 2b, as presented in Fig. 2c, exhibits the discontinuous lattice fringes, characteristic of the mesoporous structure. The Fast Fourier Transform (FFT) pattern taken from the HRTEM image, as shown in the inset of Fig. 2c, reveals that the (2 0 0) plane with the interplanar distance of 0.58 nm parallels to the growth direction of the nanobelt, and the preferential growth direction is along the normal of the (0 2 0) plane.

Fig. 3a presents the TEM micrograph of the 0.015Fe–30%TiO_2 NPs/TiO_2 NBs composite, exhibiting the deposition of the 5–10 nm

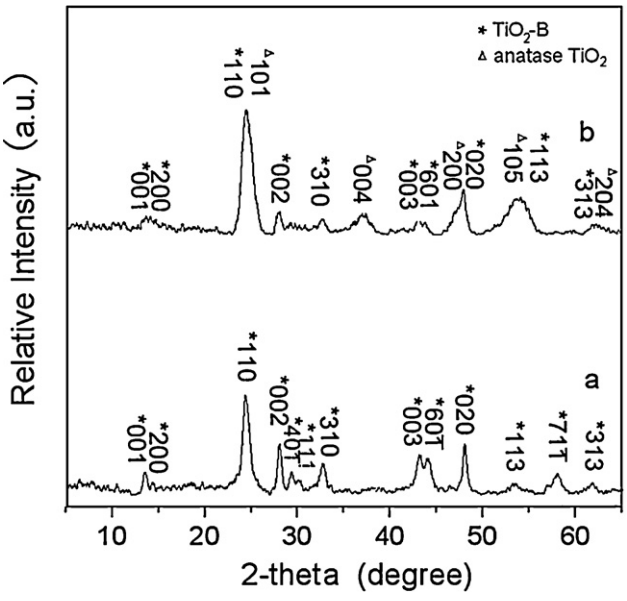

Fig. 1. XRD patterns of (a) monolinc TiO_2 NBs and (b) Fe–TiO_2 NPs/TiO_2 NBs composite.

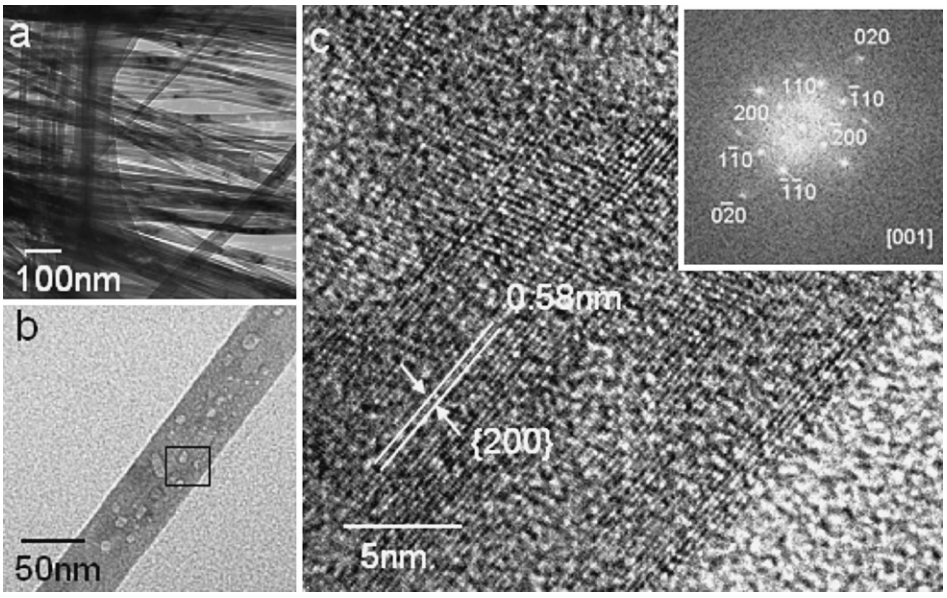

Fig. 2. (a) TEM micrograph of TiO_2 NBs with low magnification, (b) TEM micrograph of a TiO_2 NB with high magnification and (c) HRTEM image taken from the marked region in (b), inset shows its FFT pattern.

sized anatase TiO_2 NPs on the surface of the TiO_2 NB. In the HRTEM image taken from the marked region shown in Fig. 3b, sharp interface between the TiO_2 NB and the coupled TiO_2 NP is observed which makes the transition of charges possible. TEM micrographs presented in Fig. 4 display the evolution of the TiO_2 NPs layer on the surface of TiO_2 NB with increasing of the TiO_2 NPs content in the composite. For the sample with $y = 10\%$ (Fig. 4a), the TiO_2 NPs disperse independently on the surface of the TiO_2 NB. When y increases to 30%, numerous TiO_2 NPs aggregate together, forming a mesoporous layer (which was further testified by the N_2 adsorption–desorption analysis), as shown in Fig. 4b. Further increase y to 50%, the layer thickness increases accordingly (Fig. 4c). All the diffraction signals in the selected area electron diffraction (SAED) pattern taken from the marked region in Fig. 4c, as presented in Fig. 4d, are ascribed to the anatase TiO_2. While EDS spectrum (Fig. 4e) taken from the same region reveals the existence of O, Ti and Fe elements (the Cu and C peaks are from the copper grid used to support the TEM specimen), suggesting that Fe ions are incorporated in the TiO_2 crystals.

3.2. N_2 adsorption–desorption analysis

To characterize the specific surface area and porosity of the as-prepared nano-composite, the N_2 adsorption–desorption analysis was carried out. The nitrogen adsorption–desorption isotherms of the 0.015Fe–$y$$TiO_2$ NPs/TiO_2 NBs samples with Fe–TiO_2 NPs content y ranging from 0 to 50% are shown in Fig. 5. All the five samples exhibit similar adsorption–desorption isotherms that could be classified as type III with type H_3 hysteresis loop, indicating the porous aggregates of particles according to the IUPAC classification [26]. The dramatic increase in nitrogen uptake and a hysteresis loop appear at $0.8 < P/P_0 < 1.0$, due to the capillary condensation inside the mesopores [27]. The inset of Fig. 5 shows the BET surface area of the sample which increases monotonously with Fe–TiO_2 NPs content y.

The BJH pore size distribution curves of the nano-composites with various Fe–TiO_2 NPs contents y are shown in Fig. 6. The pore size distributions are unimodal with a broad peak located around 15 nm for the samples with $y = 0$ and 20%, while it changes to bimodal, with one broad peak at 15 nm and another sharp

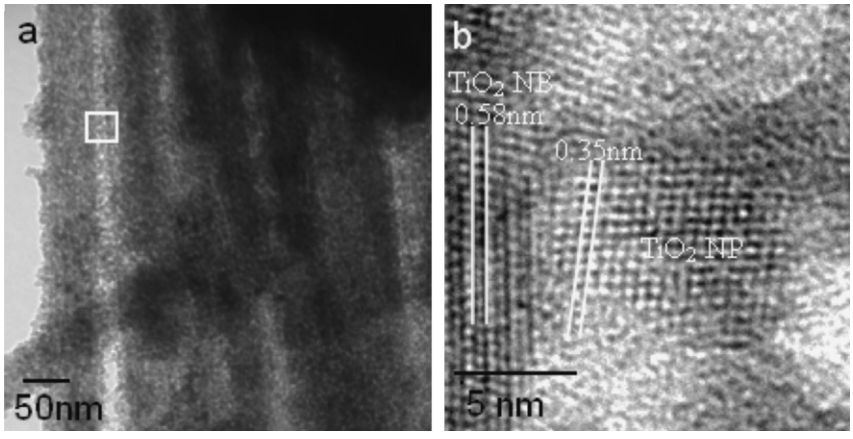

Fig. 3. TEM micrograph of 0.015Fe–30%TiO_2 NPs/TiO_2 NBs sample and (b) HRTEM image taken from the marked region in (a) showing a TiO_2 NP coupled to the surface of a TiO_2 NB.

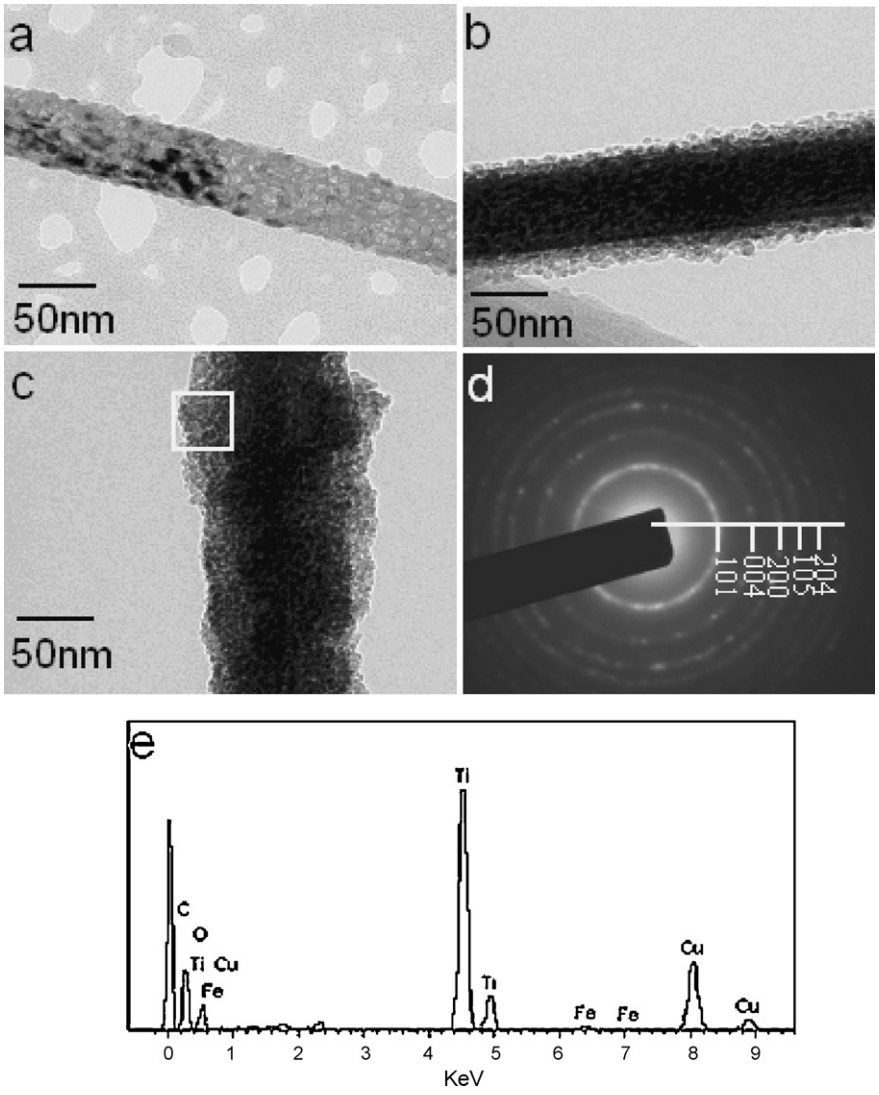

Fig. 4. TEM micrographs showing TiO_2 NB coupling with TiO_2 NPs, with y equals to (a) 10%, (b) 30%, and (c) 50%. (d) and (e): SAED pattern and EDS spectrum taken from the marked region in (c).

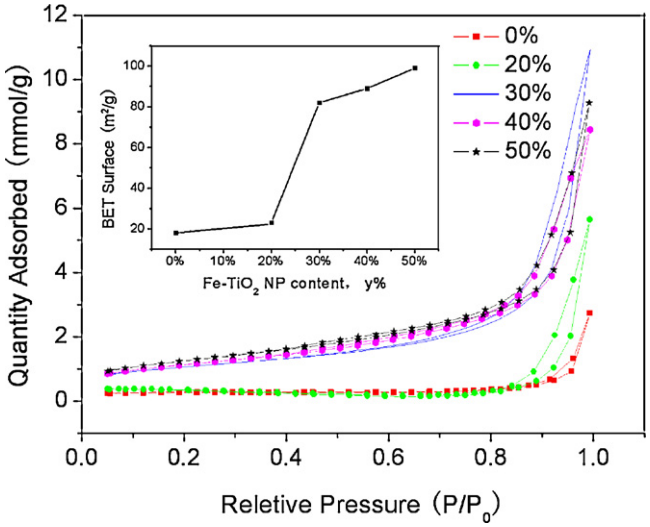

Fig. 5. Nitrogen adsorption-desorption isotherms of 0.015Fe–$y$$TiO_2$ NPs/TiO_2 NBs samples with y ranging from 0 to 50%; inset shows BET surface area versus y.

peak at 3.5 nm, for the composites with y = 30, 40 and 50%. The broad peak around 15 nm is ascribed to the porous feature of the TiO_2(B) nanobelts. When y achieves 30%, the quantity of the TiO_2 NPs becomes so huge that they aggregate together to form a TiO_2 layer with additional tiny porous structure (the mean pore size is about 3.5 nm) originated from the intergaps between the TiO_2 NPs. The 3.5 nm peak intensifies with y further increased to 40 and 50%, owing to the increase in these new tiny pores resulted from the thickening of the TiO_2 NPs layer. Based on the N_2 adsorption–desorption analyses stated above, obviously, the surface mesoporous structure of the nano-composites could be classified basically into two types: one is incompact with small BET surface area, reflecting the "loose" surface porous characteristic of the precursor TiO_2 NBs, and the other is much more compact with larger BET surface area resulting from the "serried" aggregation of the TiO_2 NPs.

3.3. UV–vis diffuse reflectance measurements

The UV–vis diffuse reflectance spectra of the xFe–30%TiO_2 NPs/TiO_2 NBs samples with x ranging from 0 to 0.025 are presented in Fig. 7. Remarkably, the absorption edge red-shifts from UV into visible region with increase of Fe doping content, which,

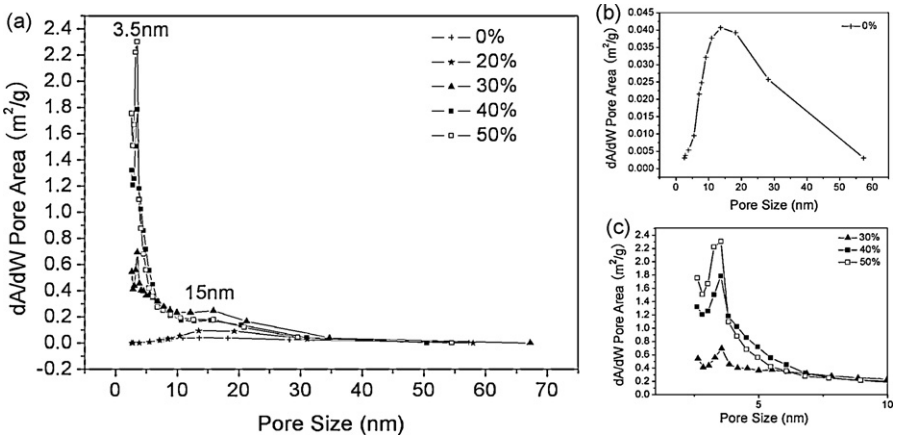

Fig. 6. (a) BJH pore size distribution curves of 0.015Fe–yTiO$_2$ NPs/TiO$_2$ NBs samples with y ranging from 0 to 50%, (b) lengthwise magnified curve of y = 0 sample and (c) magnified portions around 3.5 nm of curves from y = 30, 40, and 50%, samples.

supported by the EDS and SAED results stated above, evidences the incorporation of Fe ions into the TiO$_2$ lattices in the Fe–TiO$_2$ NPs [18,28].

Fig. 8 is the UV–vis diffuse reflectance spectra of the 0.015Fe–yTiO$_2$ NPs/TiO$_2$ NBs samples with various TiO$_2$ NPs contents y. For the pure TiO$_2$(B) nanobelt with y = 0, a strong absorption locating at the wavelength less than 400 nm was observed due to the interband transition [29]. With increase of the Fe–TiO$_2$ NPs content in the composite, the absorbance intensifies, especially in the visible region from 400 to 500 nm. The band structure of the TiO$_2$(B) phase is calculated by the Materials Studio software based on its atomic configuration, as shown in Fig. 9. Based on the interband transition, TiO$_2$(B) is considered as an indirect semiconductor. The bandgap, E_g, is usually estimated from the absorption edge wavelength according to the following equation:

$$\alpha = \frac{K(h\nu - Eg)^{1/n}}{h\nu}$$

where α is the absorbance, K is a constant, n equals 2 for the direct transition and 1/2 for the indirect transition [30]. From the plot of $(\alpha h\nu)^n$ versus energy $(h\nu)$ shown in the inset of Fig. 8, the bandgap of TiO$_2$(B) is evaluated to be 3.24 eV, in consistent with the previously reported result [21].

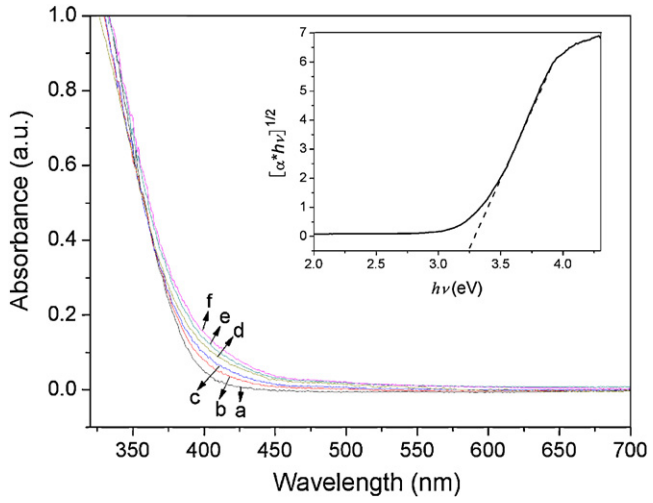

Fig. 8. UV–vis diffuse reflectance spectra of 0.015Fe–yTiO$_2$ NPs/TiO$_2$ NBs samples with various Fe–TiO$_2$ NPs contents: (a) y = 0; (b) y = 10%; (c) y = 20%; (d) y = 30%; (e) y = 40%; and (f) y = 50%; inset shows plot of $(\alpha h\nu)^{1/2}$ versus energy $(h\nu)$.

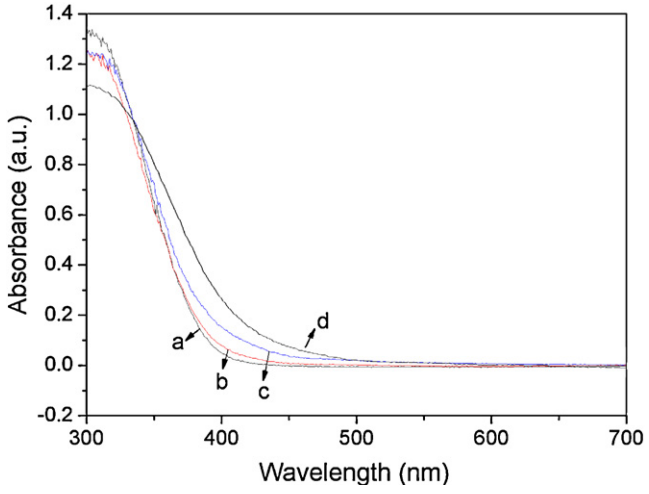

Fig. 7. UV–vis diffuse reflectance spectra of xFe–30%TiO$_2$ NPs/TiO$_2$ NBs samples with various Fe doping contents: (a) x = 0, (b) x = 0.005, (c) x = 0.015 and (d) x = 0.025.

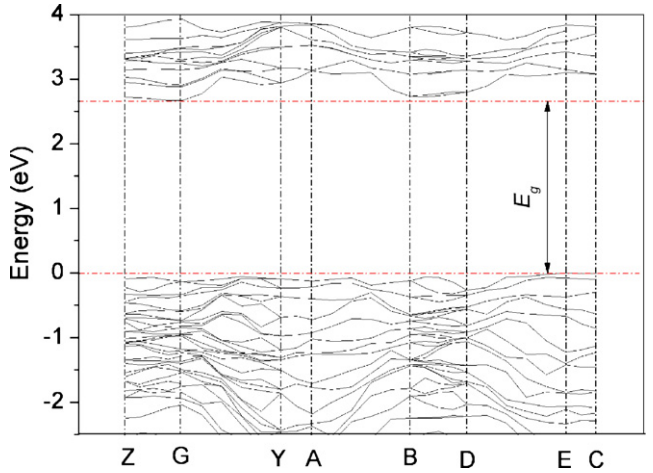

Fig. 9. Band structure of TiO$_2$(B) phase calculated by Materials Studio software based on its atomic configuration. Z, G, Y, A, B, D, E and C denote some of the high symmetry points in the brillouin zone. Their coordinates in k space are Z (0 0 0.5), Y (0 0.5 0), G (0 0 0), Y (0 0.5 0), A (−0.5 0.5 0), B (−0.5 0 0), D (−0.5 0 0.5), E (−0.5 0.5 0.5) and C (0 0.5 0.5).

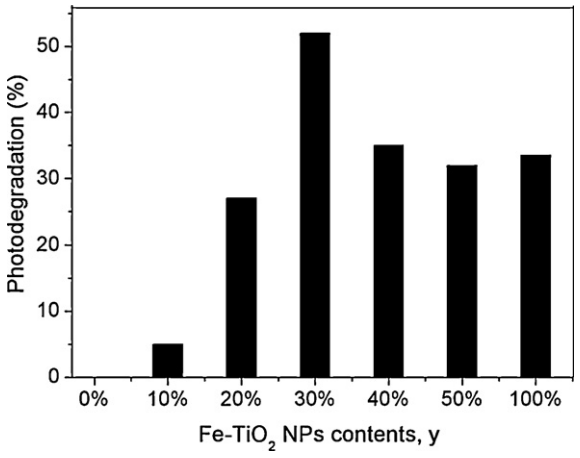

Fig. 10. Photocatalytic degradation ratio of MO under visible light irradiation over 0.015Fe–yTiO$_2$ NPs/TiO$_2$ NBs composites with various TiO$_2$ NPs contents y.

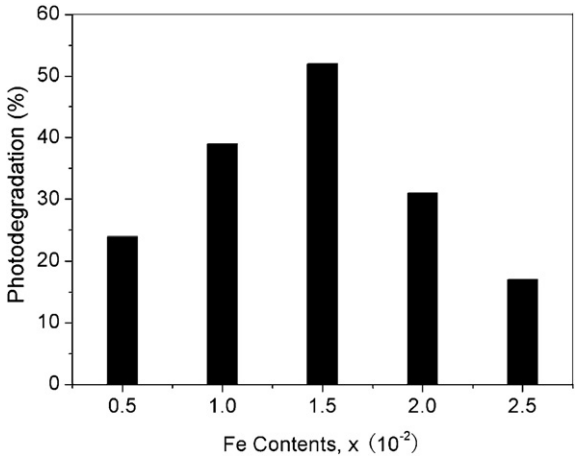

Fig. 12. Photocatalytic degradation ratio of MO under visible light irradiation over xFe–30%TiO$_2$ NPs/TiO$_2$ NBs composites with various Fe doping contents x.

3.4. Visible light photocatalysis tests

The measured MO photodegradation ratios of the 0.015Fe–yTiO$_2$ NPs/TiO$_2$ NBs composites with various TiO$_2$ NPs contents under visible light irradiation are presented in Fig. 10. Obviously, the composite exhibits the Fe–TiO$_2$ NPs content dependent visible light photocatalysis. The photocatalytic activity is completely absent in the pure TiO$_2$ NBs, and it increases with the Fe–TiO$_2$ NPs content changing gradually from 10 to 30%. However, it decreases when the Fe–TiO$_2$ NPs content excesses 30%. The composite with y = 30% yields the highest photocatalytic efficiency, with the degradation ratio of the 10^{-5} M MO achieving 52% after 5 h irradiation.

The changes of the band configurations for anatase TiO$_2$ and TiO$_2$(B) resulted from the Fe doping and the anatase TiO$_2$/TiO$_2$(B) coupling are illustrated schematically in Fig. 11. As we know, both anatase TiO$_2$ and TiO$_2$(B) are n-type semiconductors with similar bandgap energy of 3.2 eV [21,23], and their Fermi levels are all near the conduction bands (the Fermi level, $E_{F\ TiO_2(B)} = 1.11$ V [31] and $E_{F\ anatase} = 0.51$ V [32]). After Fe^{3+} doping, anatase TiO$_2$ turns to be p-type semiconductor with Fermi level close to its valence band [33–35]. After Fe-doped anatase TiO$_2$ NPs/TiO$_2$(B) NBs coupling, electrons migrate from the TiO$_2$(B) NBs to the Fe-doped anatase TiO$_2$ NPs, while holes migrate in a reverse direction, resulting in an equivalence of the TiO$_2$(B) Fermi level and the anatase TiO$_2$ one. Meanwhile, an accumulation of negative electrons in the anatase TiO$_2$ region and positive holes in the TiO$_2$(B) region adjacent to the interface is created, which sets up an internal electrostatic field between TiO$_2$(B) and anatase TiO$_2$ [36]. A p–n junction is thus formed at the interface. Under visible light irradiation, the electron-hole pairs are generated in the Fe-doped anatase TiO$_2$. Driven by the internal electrostatic field, the electrons transfer to the TiO$_2$(B) side, which reduces the probability of the electron–hole recombination, and promotes the photocatalytic activity of the Fe-doped TiO$_2$ NPs/TiO$_2$ NBs nano-composite. For the results shown in Fig. 10, since the Fe-doped TiO$_2$ is the sole component in the composite sensitive to the visible light, the enhancing of the composite catalytic activity with y when y is relative small (<30%) is obviously understandable. As for the decrease of the catalysis in the samples with y > 30%, it could be explained by the over-thickening of the Fe–TiO$_2$ NPs layers on the TiO$_2$ NBs surfaces which on one hand reduces the quantity of the photogenerated carriers arriving the interfaces, and on the other hand, brings difficulties for the reactants to reach the surfaces of the nanobelts.

Fig. 12 shows the photodegradation capability of the 10^{-5} M MO under visible light irradiation over the xFe–30%TiO$_2$ NPs/TiO$_2$ NBs composites with various Fe contents in the TiO$_2$ NPs. The photocatalytic activity increases with gradual rising of Fe doping content from 0.005 to 0.015, and turns to decrease rapidly when Fe content excesses 0.015. The catalyst with x = 0.015 exhibits the highest photocatalytic efficiency. This result is explained as follows: with increase of Fe content in the TiO$_2$ NPs, the absorption edge of TiO$_2$ red-shifts to longer wavelength, thus more carriers are generated under visible light irradiation, which naturally induces the increase

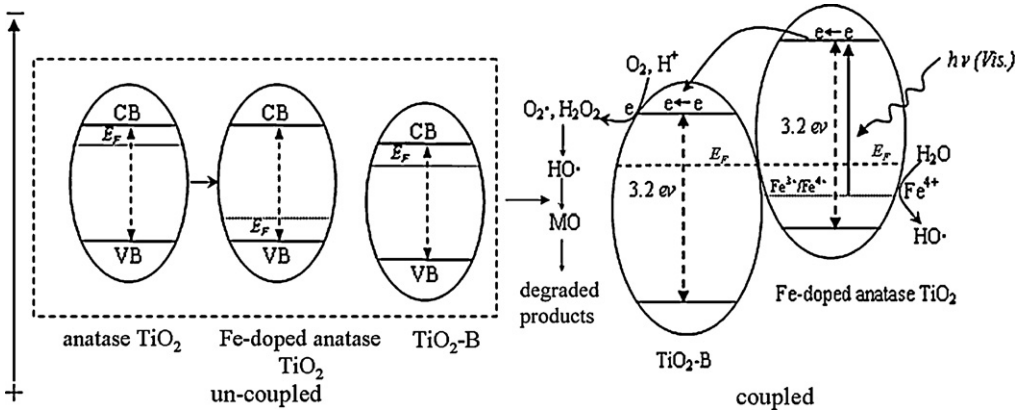

Fig. 11. Changes of band configurations for anatase TiO$_2$ and TiO$_2$(B) resulted from Fe doping and anatase TiO$_2$/TiO$_2$(B) coupling. Mechanism for MO degradation under visible light irradiation is also schematically illustrated.

of the photocatalytic efficiency. However, since Fe^{4+} ions may also act as the recombination centers for the photogenerated carriers [18], when the doped Fe in TiO_2 exceeds a certain concentration, the photocatalysis turns to be weakened due to the decrease of the photogenerated carriers [28,37]. The optimum Fe content here is obviously higher than that for the photocatalyst with Fe-doped anatase TiO_2 NPs loading on the hollow glass microbeads (which is 0.010) reported in our previous work [28], probably ascribing to the charge separation effect of the interfaces between the TiO_2 NPs and the TiO_2(B) NBs which reduces the Fe^{4+} induced recombination ratio of the photogenerated charges.

4. Conclusions

The nano-composite coupling Fe-doped anatase TiO_2 nanoparticles to TiO_2(B) nanobelts was prepared by solution synthesis. The composite has mesoporous surface structure originating from the serried aggregation of the TiO_2 nanoparticles, and exhibits desirable visible light photocatalytic activity dependent on both the content of the anatase TiO_2 and its Fe doping level. For the optimized composite, the photodegradation ratio of the 10^{-5} M MO aqueous solution achieves 52% under 500 W visible light irradiation for 5 h.

Acknowledgments

This work was financially supported by projects of Natural Science Foundation of China (10974201, 50902130), and State Key Laboratory of Optoelectronic Materials and Technologies (KF2008-ZD-05).

References

[1] A. Fujishima, T.N. Rao, D.A. Tryk, J. Photochem. Photobiol. C: Photochem. Rev. 1 (2000) 1.
[2] O. Carp, C.L. Huisman, A. Reller, Prog. Solid State Chem. 32 (2004) 33.
[3] M.R. Hoffmann, S.T. Martin, W. Choi, D.W. Bahnemann, Chem. Rev. 95 (1995) 69.
[4] K. Tsujimaru, Eco-Mater. Process. Des VII 510 (2006) 5.
[5] D.F. Ollis, E. Pellizzetti, N. Serpone, Environ. Sci. Technol. 25 (1991) 1522.
[6] J. Wu, S. Hao, J. Lin, M. Huang, Y. Huang, Z. Lan, P. Li, Cryst. Growth Des. 8 (2008) 247.
[7] W.Y. Su, Y.F. Zhang, Z.H. Li, L. Wu, X.X. Wang, J.Q. Li, X.Z. Fu, Langmuir 24 (2008) 3422.
[8] J. Zhang, Q. Xu, Z. Feng, M. Li, C. Li, Angew. Chem., Int. Ed. 47 (2008) 1766.
[9] A. Testino, I.B. Bellobono, V. Buscaglia, C. Canevali, M. D'Arienzo, S. Polizzi, R. Scotti, F. Morazzoni, Am. J. Chem. Soc. 129 (2007) 3564.
[10] T. Kawahara, Y. Konishi, H. Tada, N. Tohge, J. Nishii, S. Ito, Angew. Chem., Int. Ed. 41 (2002) 2811.
[11] Z. Zhenga, H. Liua, J. Yeb, J. Zhaob, E.R. Waclawika, H. Zhu, J. Mol. Catal. A: Chem. 316 (2010) 75.
[12] H. Luo, C. Wang, Y. Yan, Chem. Mater. 15 (2003) 3841.
[13] W. Li, C. Liu, Y. Zhou, Y. Bai, X. Feng, Z. Yang, L. Lu, X. Lu, K.Y. Chan, J. Phys. Chem. C 112 (2008) 20539.
[14] R.I. Bickley, T. Gonzalez-Carreno, J.S. Lees, L. Palmisano, J.D. Tilley, J. Solid State Chem. 92 (1991) 178.
[15] A.K. Datye, G. Riegel, J.R. Bolton, M. Huang, M.R. Prairie, J. Solid State Chem. 115 (1995) 236.
[16] D.C. Hurum, K.A. Gray, J. Phys. Chem. B 109 (2005) 977.
[17] H. Xu, L. Zhang, J. Phys. Chem. C 113 (2009) 1785.
[18] W. Choi, A. Termin, M.R. Hoffmann, J. Phys. Chem. 98 (1994) 13669.
[19] Q.X. Deng, M.D. Wei, X.K. Ding, L.L. Jiang, B.H. Ye, K.M. Wei, Chem. Commun. (2008) 3657.
[20] Q. Wang, Z.H. Wen, J.H. Li, Adv. Funct. Mater. 16 (2006) 2141.
[21] G. Betz, H. Tributsch, R.J. Marchand, Appl. Electrochem. 14 (1984) 315.
[22] G. Nuspl, K. Yoshizawab, T.J. Yamabe, Mater. Chem. 7 (1997) 2529.
[23] A.R. Armstrong, G. Armstrong, J. Canales, P.G. Bruce, Angew. Chem., Int. Ed. 43 (2004) 2286.
[24] A.K. Chakraborty, Z. Qi, S.Y. Chai, C. Lee, S.Y. Park, D.J. Jang, W.I. Lee, Appl. Catal. B 93 (2010) 368.
[25] T. Kasuga, M. Hiramatsu, A. Hoson, T. Sekino, K. Niihara, Adv. Mater. 15 (1999) 1307.
[26] F. Rouquerol, J. Rouquerol, K. Sing, Adsorption by Powders and Porous Solids: Principles, Methodology, and Applications, Academic Press, San Diego, 1999.
[27] P.T. Tanev, M. Chibwe, T.J. Pinnavaia, Nature 368 (1994) 321.
[28] L. Cui, Y. Wang, M. Niu, G. Chen, Y. Cheng, J. Solid State Chem. 182 (2009) 2785.
[29] W.Z. Zhang, M. Froba, J.L. Wang, P.T. Tanev, J. Wong, T.J. Pinnavaia, J. Am. Chem. Soc. 118 (1996) 9164.
[30] G. Kortuem, Reflectance Spectroscopy: Principles, Methods, Applications, Springer–Verlag, Berlin–Heidelberg, 1969.
[31] G. Wang, Q. Wang, W. Lu, J.H. Li, J. Phys. Chem. B 110 (2006) 22029.
[32] M. Gartner, V. Dremov, P. Muller, H. Kisch, Chem. Phys. Chem. 6 (2005) 714.
[33] Z. Ambrus, N. Balazs, T. Alapi, G. Wittmann, P. Sipos, A. Dombi, K. Mogyorosi, Appl. Catal. B 81 (2008) 27.
[34] L.C. Liau, C.C. Lin, Appl. Surf. Sci. 253 (2007) 8798.
[35] A.R. Bally, E.N. Korobeinikova, P.E. Schmid, F.L. Levy, F. Bussy, J. Phys. D 31 (1998) 1149.
[36] R.L. Anderson, Solid State Electron. 5 (1962) 341.
[37] A. Di Paola, G. Marci, L. Palmisano, M. Schiavello, K. Uosaki, B. Ohtani, J. Phys. Chem. B 106 (2002) 637.